



THE UNIVERSITY *of* EDINBURGH

Edinburgh Research Explorer

## Directional balancing for seismic and general wavefield interferometry

**Citation for published version:**

Curtis, A & Halliday, D 2010, 'Directional balancing for seismic and general wavefield interferometry' Geophysics, vol. 75, no. 1. DOI: 10.1190/1.3298736

**Digital Object Identifier (DOI):**

[10.1190/1.3298736](https://doi.org/10.1190/1.3298736)

**Link:**

[Link to publication record in Edinburgh Research Explorer](#)

**Document Version:**

Publisher's PDF, also known as Version of record

**Published In:**

Geophysics

**Publisher Rights Statement:**

Published by the Society of Exploration Geophysicists (2010)

**General rights**

Copyright for the publications made accessible via the Edinburgh Research Explorer is retained by the author(s) and / or other copyright owners and it is a condition of accessing these publications that users recognise and abide by the legal requirements associated with these rights.

**Take down policy**

The University of Edinburgh has made every reasonable effort to ensure that Edinburgh Research Explorer content complies with UK legislation. If you believe that the public display of this file breaches copyright please contact [openaccess@ed.ac.uk](mailto:openaccess@ed.ac.uk) providing details, and we will remove access to the work immediately and investigate your claim.



Publisher PDF- Deposited in Edinburgh University Research Archive. Copyright (2010) Society of Exploration Geophysicists.

Cite As: Curtis, A & Halliday, D 2010, 'Directional balancing for seismic and general wavefield interferometry' Geophysics, vol 75, no. 1. DOI: 10.1190/1.3298736

## Directional balancing for seismic and general wavefield interferometry

Andrew Curtis<sup>1</sup> and David Halliday<sup>2</sup>

### ABSTRACT

In passive seismic interferometry using naturally occurring, heterogeneous noise sources and in active-source seismic interferometry where sources can usually only be distributed densely on the exterior of solid bodies, bias can be introduced in Green's function estimates when amplitudes of energy have directional variations. We have developed an algorithm to remove bias in Green's function estimates constructed using seismic interferometry when amplitudes of energy used have uncontrollable directional variations. The new algorithm consists of two parts: (1) a method to measure and adjust the amplitudes of physical, incoming energy using an array of receivers and (2) a method to predict and remove nonphysical energy that remains (and can be accentuated) in interferometrically derived Green's functions after applying the method in step 1. To accomplish step 2, we have created two data-driven methods to predict the nonphysical energy using direct computation or move-out-based methods, and a way to suppress such energy using (in this case) helical least-squares filters. Two-dimensional acoustic scattering examples confirm the algorithm's effectiveness.

### INTRODUCTION

Seismic interferometry has become an important and popular approach to synthesize and analyze wavefields. Energy recorded at two receivers from an array of transient or noise sources spanning a boundary surface surrounding the receiver pair can be converted by simple crosscorrelation operations into approximations to the inter-receiver Green's function. This Green's function is the signal that would have been recorded at one receiver if the other receiver had instead been an impulsive source.

Although Claerbout (1968) proves this method in a 1D medium for the case of both receivers being at the same location (i.e., using

only a single receiver), Wapenaar (2003, 2004), van Manen et al. (2005, 2006), and Wapenaar and Fokkema (2006) prove the method mathematically for 3D acoustic and elastic media, showing that, in principle, monopolar (e.g., pressure) and dipolar (e.g., particle velocity/displacement) sources are required on the bounding surface.

Van Manen et al. (2005, 2006, 2007) show how the impulsive or noise-source versions of this theory create a new computational schema with which synthetic wavefields between receivers can be modeled flexibly. In an industrial seismic setting, Bakulin and Calvert (2004, 2006) show that in the case of receivers located in a subsurface horizontal borehole and sources located on the surface above the borehole, seismic interferometry can be used to redatum sources into the borehole, removing many undesirable near-surface-related effects from the seismic data. Draganov et al. (2007) show that major body-wave components of Green's functions could be estimated using background (passive) noise records in a particularly quiet area. Curtis et al. (2006), Dong et al. (2006), Halliday et al. (2007, 2008), and Halliday and Curtis (2008, 2009) illustrate that in a seismic setting, surface waves are particularly well recovered and can be used as part of a general surface-wave removal algorithm for cases where surface waves arrive simultaneously with important body-wave information.

In all of these applications, Green's functions are constructed between a pair of receivers within the medium. One of the receivers is effectively converted into a virtual (imagined) source, the energy from which is recorded at the other receiver. The geometry required for exact seismic interferometry is illustrated in Figure 1. If monopolar and dipolar impulsive sources on the boundary  $S$  are fired sequentially, the signals recorded at any pairs of receivers in its interior are Green's functions between the boundary and the receiver locations. Wapenaar (2003, 2004), van Manen et al. (2005, 2006), and Wapenaar and Fokkema (2006) show that in the acoustic case the inter-receiver Green's function  $G(\mathbf{x}_1, \mathbf{x}_2)$  between  $\mathbf{x}_1$  and  $\mathbf{x}_2$  (with source at  $\mathbf{x}_1$ ) is obtained by

Manuscript received by the Editor 5 November 2008; revised manuscript received 16 July 2009; published online 25 February 2010.

<sup>1</sup>The University of Edinburgh, School of GeoSciences, Grant Institute, Edinburgh, U. K.; Edinburgh Collaborative of Subsurface Science and Engineering, Edinburgh, U. K.; and WesternGeco London Technology Centre, West Sussex, U. K. E-mail: andrew.curtis@ed.ac.uk.

<sup>2</sup>Formerly University of Edinburgh, School of Geosciences, Grant Institute, Edinburgh, U. K., and Edinburgh Collaborative of Subsurface Science and Engineering, Edinburgh, U. K.; presently Schlumberger Cambridge Research, Cambridge, U. K. E-mail: david.f.halliday@googlemail.com.  
© 2010 Society of Exploration Geophysicists. All rights reserved.

$$G(\mathbf{x}_1, \mathbf{x}_2) + G^*(\mathbf{x}_1, \mathbf{x}_2) = \oint_S \frac{-1}{j\omega\rho(\mathbf{x})} [G^*(\mathbf{x}, \mathbf{x}_1) \partial_i G(\mathbf{x}, \mathbf{x}_2) - \partial_i G^*(\mathbf{x}, \mathbf{x}_1) G(\mathbf{x}, \mathbf{x}_2)] n_i d^2\mathbf{x}, \quad (1)$$

where the frequency dependence of  $G(\mathbf{x}_1, \mathbf{x}_2)$  is implicit. Here,  $\mathbf{x}_1$  and  $\mathbf{x}_2$  are the two receiver positions,  $\mathbf{x}$  is the integration variable that traces source positions on bounding surface  $S$ ,  $\rho(\mathbf{x})$  is the density,  $\mathbf{n}$  is the unit normal vector to  $S$  at any point  $\mathbf{x}$ ,  $j$  is the square root of  $-1$ , and there is implicit Einstein summation over  $i$ . The Green's functions in this formula are specifically those for a volume injection rate source at  $\mathbf{x}_1$  and a received pressure field at  $\mathbf{x}_2$ , and the derivative Green's functions correspond to dipolar sources at the boundary  $S$ . If displacement Green's functions are used, the difference between the Green's function and its conjugate (rather than their sum) is obtained on the left of equation 1.

When applying equation 1, the sources are implemented separately, as is the case in exploration geophysics where active sources are used. When passive (i.e., uncontrolled) sources are used, one can consider that those sources act simultaneously. In this case, time averaging is required to cancel cross-terms appearing as a result of crosscorrelating different sources (see Snieder [2004] and van Manen et al. [2006]).

In the following, we consider the exact application of equation 1 for acoustic waves; however, given the relationships in equation 1 and other forms of the interferometric integral, our results can be interpreted in terms of active- and passive-source interferometry (Wapenaar and Fokkema, 2006). Van Manen et al. (2006) and Wapenaar and Fokkema (2006) give equivalents of these formulas for elastic-wave propagation, and Slob and Wapenaar (2007) and Slob

et al. (2007) give equivalents for electromagnetic-wave propagation. Under a unified formulation of the theory, other types of Green's functions can be retrieved, such as electrokinetic Green's functions in poroelastic or piezoelectric media (Wapenaar et al., 2006). Wapenaar and Fokkema (2006) show by using the Sommerfeld radiation condition (Born and Wolf, 1999) that the source requirements for integrals such as equation 1 can be relaxed such that only monopole sources are required. Hence, although the examples in this paper concern acoustic-wave propagation and both monopole and dipole sources, our method can be applied using equivalent formulae for other wave-propagation regimes and for single source types.

To obtain the Green's functions using equation 1, Green's functions from the boundary must be known; hence, the medium within  $S$  has been illuminated evenly from all directions. In practical situations with impulsive sources, this implies that energy from all boundary sources should be normalizable to unit impulses. For random noise sources, it implies that the total power radiated by each source be equal.

Although normalization might be possible for actual sources fired given source signature recordings, nobody has described how to do this correctly for cases in which the source recording is inaccurate or incomplete, or for missing boundary sources such as is the norm in industrial exploration seismology where sources are generally confined to the near surface of the earth (and, hence, do not surround the receiver pair at depth). Nor has any method been presented to correct the general case of seismic interferometry using passive- or background-noise sources where these could each have quite different source-time functions and magnitudes, such as is common in passive-noise seismology (Stehly et al., 2006). Hence, from numerical experiments, we know that in such cases strong biases will be introduced in the interferometric Green's functions (van Manen et al., 2005, 2006; Wapenaar, 2006; Vasconcelos and Snieder, 2008a, 2008b).

One method of correction proposed by Douma and Snieder (2006) relies on a statistical model of the noise, which is generally unknown in exploration-geophysical applications. In another method, Mehta et al. (2007) show that wavefield separation into up- and downgoing components prior to interferometry and crosscorrelation of down- and upgoing wavefields could help to suppress spurious overburden-related effects in the horizontal well-based method of Bakulin and Calvert (2004, 2006). Douma and Snieder (2006) also apply the method to seabed data to remove the effects of sea-level changes. However, neither method creates uniform noise directionality, and neither generalizes in an obviously robust way to 3D heterogeneous media with a less linear source or receiver array.

Van der Neut and Bakulin (2008) propose a method by which the amplitude radiation pattern of a virtual source can be estimated and corrected using wavefield separation prior to directional balancing. Their approach is for a linear array of sensors in the subsurface, where the array lies inside a homogeneous layer and spans virtual source and receiver locations. The method simultaneously adjusts directionality and removes the effect of any overburden on the estimated wavefields in a fashion similar to the method of Mehta et al. (2007).

Another method is introduced by Wapenaar et al. (2008), who propose the use of multidimensional deconvolution (MDD) of separated passive wavefields. They show that, theoretically, MDD will solve the problem of irregular source strength and irregular amplitude. However, this requires data that can be processed to separate

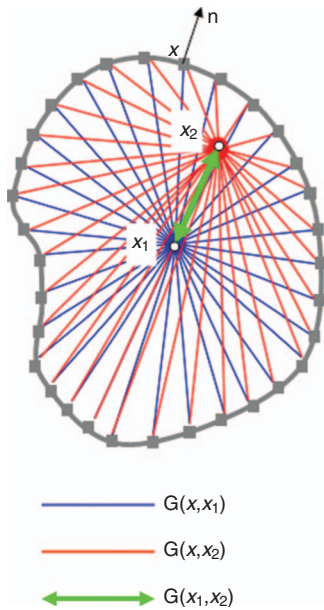


Figure 1. Geometry of various quantities and vectors used for wave-field interferometry. If impulsive sources at locations  $\mathbf{x}$  around the boundary are recorded at two receivers at  $\mathbf{x}_1$  and  $\mathbf{x}_2$ , giving Green's functions represented by blue and red lines, respectively, the inter-receiver (green) Green's function can be calculated exactly using equation 1.

the wavefield into various components required for MDD — in particular, it requires that free-surface multiples be removable from the data. Wapenaar et al. (2008) achieve this by assuming that each source is transient, rather than continuous as might be the case for passive noise data, and they remove multiples by time-windowing recorded data.

In this paper, we present a method that corrects for directional bias in interferometric estimates where the sources on the boundary surface  $S$  have variable source strength. This method requires no knowledge of the background source distribution nor its time dependence; hence, it is ideal for cases where passive-seismic interferometry is applied but is equally applicable to situations using active sources. If the wavefield at either of the pair of receivers can be decomposed directionally at one of the receiver locations (e.g., by using a local receiver array), a virtual source with near-uniform directionality can be constructed using an algorithm that we call *directional balancing*. This algorithm is applicable to full wavefields (i.e., no other wavefield separation or multiple removal is required prior to its use), and it works implicitly with multidimensional arrays and (because it requires only local directional decomposition around one receiver) in heterogeneous media.

However, the method we use to correct directionality does not remove nonphysical arrivals introduced during directionally biased interferometry in heterogeneous media. Thus, we propose a second method that predicts and removes such nonphysical arrivals after directional balancing. The resulting corrected Green's function estimates show much-reduced effects of nonuniform source-strength distribution in the presence of directional bias. These estimates are therefore more appropriate for a conventional seismic-processing flow, especially where both traveltime and amplitude data are required. This is especially important where passive-seismic interferometry is used to supplement active-source data, in which case it is desirable that the passive estimates closely resemble the character of the active-source data.

We begin by detailing the directional-balancing algorithm and apply it to examples of increasing complexity, illustrating the emergence of nonphysical arrivals as the medium's complexity increases. We explain from where these arrivals originate and propose two new methods to identify them from physically propagating waves. Finally, we use least-squares filters to remove the nonphysical arrivals from the directionally balanced data.

## DIRECTIONAL BALANCING

We want to estimate a directionally unbiased (isotropic) Green's function between a virtual source at  $\mathbf{x}_1$  and a receiver at  $\mathbf{x}_2$ . At both, there are physical receivers, where  $\mathbf{x}_1$  is also surrounded by a local array of receivers  $\mathbf{x}_r$ .

To estimate correction factors to account for directional bias in the interferometric estimate, we first consider only the virtual source location  $\mathbf{x}_1$  and the surrounding local array of receivers  $\mathbf{x}_r$ . Using interferometry, we calculate all biased Green's functions  $G'(\mathbf{x}_1, \mathbf{x}_r)$  (in this paper, we apply equation 1; in practice, one may consider any interferometric integral). The functions  $G'(\mathbf{x}_1, \mathbf{x}_r)$  contain information about the local radiation pattern of the virtual source. Later, we show that if the medium is heterogeneous, the estimates contain nonphysical arrivals; hence, we assume that physical arrivals dominate the estimates in the immediate near field at early times (the following results show that this assumption is valid). We determine a local earth property model at and around the receiver array and synthetically

model wave propagation locally around the virtual source (i.e., we model only the initial radiation pattern within the array, so a simple model may be sufficient). Then, we calculate synthetic Green's functions  $G(\mathbf{x}_1, \mathbf{x}_r)$ , which are isotropic and diffraction limited (see below).

We want to find a scaling factor in some domain  $D$  that adjusts the source directionality of the biased interferometric estimates to have the same source directionality as the modeled data. As such, the method relies on having a good estimate of the earth properties (for synthetic modeling) immediately at and around the virtual-source array.

As a concrete example of the method, we consider the case where  $D$  is the frequency-wavenumber ( $f$ - $k$ ) domain and cast the problem of finding the optimal directional balancing scaling factors  $C^{\text{opt}}(\mathbf{x}_1, \mathbf{k}_r)$  to correct the directional bias as a minimization problem:

$$C^{\text{opt}}(\mathbf{x}_1, \mathbf{k}_r) = \min_{\arg C} (\|G(\mathbf{x}_1, \mathbf{k}_r) - C(\mathbf{x}_1, \mathbf{k}_r) \cdot G'(\mathbf{x}_1, \mathbf{k}_r)\|), \quad (2)$$

where  $\|\dots\|$  denotes any desired norm and the dot product on the right represents element-by-element multiplication because we are in the wave-vector rather than spatial domain (i.e., convolution in the spatial domain).

In the examples following, using noiseless synthetic data, we solve equation 2 by dividing each component of  $G$  by the same component of  $G'$  to obtain the corresponding component of  $C^{\text{opt}}$ . However, for noisy data or if any near-zero components of  $G'$  occur, an explicit minimization must be performed. Note that the  $f$ - $k$  transform is taken across the local receiver array and not across the virtual-source coordinates; hence, the coordinates change from  $\mathbf{x}_r$  to  $\mathbf{k}_r$  but not from  $\mathbf{x}_1$  to  $\mathbf{k}_1$ . Because the array is 2D in space, a 3D Fourier transform is required.

The scaling factor  $C^{\text{opt}}(\mathbf{x}_1, \mathbf{k}_r)$  that minimizes the right side of equation 2 then allows us to correct for directional bias in the interferometrically estimated Green's functions  $G'(\mathbf{x}_1, \mathbf{x}_r)$  by convolving  $C^{\text{opt}}$  with  $G'$ . However, because this operation corrects for biased directionality in energy propagating across the array around the virtual source location, it can also be used to correct  $G'(\mathbf{x}_r, \mathbf{x}_2)$  (i.e., the wave components propagating between the virtual source array  $\mathbf{x}_r$  and any other receiver  $\mathbf{x}_2$ ). This is achieved as follows.

Transforming  $G'(\mathbf{x}_r, \mathbf{x}_2)$  to  $G'(\mathbf{k}_r, \mathbf{x}_2)$  (or to any other  $D$  and using the same array of receivers at locations  $\mathbf{x}_r$ , as above) results in a local decomposition of the Green's functions  $G'(\mathbf{x}_r, \mathbf{x}_2)$  into planar components of the wavefield propagating from around the virtual source location  $\mathbf{x}_1$  to location  $\mathbf{x}_2$ . Importantly, the decomposition is made with respect to the same plane-wave basis vectors used to determine  $C^{\text{opt}}$  because the same local array is used. Therefore, because the decomposition in  $G'(\mathbf{k}_r, \mathbf{x}_2)$  is local to location  $\mathbf{x}_1$ , it also approximately represents directional components of the virtual source at  $\mathbf{x}_1$  in  $G'(\mathbf{x}_1, \mathbf{x}_2)$ .

The same real boundary sources (at locations  $\mathbf{x}$  in equation 1) are used to construct all of the above sets of Green's functions marked  $G'$  (i.e., all other than the synthetic Green's functions  $G$ ). Hence, if the virtual sources in  $G'(\mathbf{x}_r, \mathbf{x}_2)$  are directionally biased across the array, then they will have been equally biased in  $G'(\mathbf{x}_1, \mathbf{x}_r)$ . Any such bias is approximately corrected by  $C^{\text{opt}}$ . Therefore,  $C^{\text{opt}}$  can also be applied to  $G'(\mathbf{k}_r, \mathbf{x}_2)$  as



$$G''(\mathbf{k}_r, \mathbf{x}_2, \omega) = C^{\text{opt}}(\mathbf{x}_1, \mathbf{k}_r, \omega) \cdot G'(\mathbf{k}_r, \mathbf{x}_2, \omega), \quad (3)$$

where  $G''(\mathbf{k}_r, \mathbf{x}_2, \omega)$  are the corrected Green's function in the  $f-k$  domain. Transforming back to the original domain and interpolating to location  $\mathbf{x}_1$  gives  $G''(\mathbf{x}_1, \mathbf{x}_2)$ ; this is a less directionally biased estimate of  $G(\mathbf{x}_1, \mathbf{x}_2)$ .

We must interpolate to  $\mathbf{x}_1$  only because the modeling method that we use (see below) cannot model a coinciding source and receiver (there is a singularity at zero offset); other modeling approaches may not require this additional interpolation step. Also, we have chosen to implement the algorithm in a frequency-dependent manner because different frequencies of wave propagation are sensitive to different Fresnel zones in the medium.

To construct the ideal radiation pattern  $G(\mathbf{x}_1, \mathbf{x}_r)$ , we deliberately use the diffraction-limited modeling method of [van Manen et al. \(2005, 2006, 2007\)](#). These authors show that when applying seismic interferometry to noise or active source data in the very near-field of the virtual source point, the Green's function cannot be constructed exactly; the difference to the exact Green's function is attributed to the diffraction-limited nature of seismic interferometry and time reversal. This difference is related to the work of [de Rosny and Fink \(2002\)](#), who discuss the role of the diffraction limit in time-reversed imaging. Consequently, experiments show that using a nondiffraction-limited modeling method gives incorrect results in the directional-balancing algorithm because, in equation 2, the diffraction-limited  $G$  would be compared to a nondiffraction-limited  $G'$ . However, by using the interferometric modeling method of [van Manen et al. \(2005, 2006\)](#), we ensure that our modeled radiation pattern in  $G$  is consistent with the limitations of the interferometric estimates  $G'$  themselves in the very near field.

In the directional-balancing algorithm, we assume that the ideal source radiation is isotropic. Of course, any other desired source radiation pattern could be modeled in  $G(\mathbf{x}_1, \mathbf{x}_r)$  and approximated by the algorithm in equations 2 and 3. We also choose the Fourier domain for  $D$  because it is commonly used for processing. However, other domains might be chosen if preferred. The radon domain in

particular might provide equally good results when balancing directional amplitudes.

Equation 2 can be viewed as a multidimensional spatial deconvolution operation, where the estimated source-radiation field  $G'$  is deconvolved from the desired source-radiation field  $G$  in order to estimate  $C^{\text{opt}}$ . However, this should not be confused with the method of interferometry by multidimensional deconvolution (MDD) of [Wapenaar et al. \(2008\)](#). In that specific approach to interferometry, Wapenaar et al. find a set of relations that should hold between wavefields recorded with and without a free surface present. They convert real data recorded at the earth's free surface into the corresponding wavefields without the free surface (by removing free-surface multiples) and solve the set of relations to find the desired Green's functions with the free surface present. However, their method requires that the data without the free surface be constructed correctly, and removing multiples by time windowing (as they perform) requires that sources be temporally limited.

We instead construct a set of relations between the recorded, biased wavefield and a desired, modeled wavefield (equation 2). We solve these relations for the desired Green's functions that match those characteristics of the modeled field. In the following examples, we show that if the latter wavefield is only modeled in the very near-field of the virtual source, then application of  $C^{\text{opt}}$  as in equation 3 ensures that the radiation characteristics of the virtual source match those of the modeled source (in the examples below, this ensures that the virtual source radiation pattern is isotropic). Our method therefore does not require multiple removal, nor does it require that sources be temporally limited.

## Application of directional balancing

To illustrate the directional-balancing algorithm, we use a series of synthetic acoustic models. We first use a homogeneous acoustic example to step through the application of the algorithm and to illustrate that it can correct for a nonuniform boundary-source-amplitude distribution. We then consider more complex examples.

### Model parameters

We use a 2D geometry (Figure 2), consisting of a circular boundary of sources (radius 200 m, sources separated by 4 m) with a  $20 \times 20$  array of receivers (4 m separation) around the virtual source location. The boundary is centered on  $[0,0]$  m, and the array is centered on  $[0,70]$  m. At the center of the array, we place an additional receiver at the virtual source location, i.e., the location where we want to apply our corrections (Figure 3). We have chosen this size of virtual source array because we found that a  $20 \times 20$  square array of receivers gives good result. The array geometry has not been optimized in any way. We choose a line of 31 receivers, ranging from  $[-150, -80]$  m to  $[150, -80]$  m with a separation of 10 m, on which we want to record energy from the virtual source. The wave propagation velocity of the medium is 750 m/s, and a Ricker wavelet with center frequency of 30 Hz allows the source separation of 4 m to be well sampled (unaliased).

We define a nonuniform source strength by the function  $T_j$ , where  $T$  is the strength of the source and  $j$  denotes the boundary location. Initially, we use a cosine function with a minimum value of one and a maximum value of two to define this variation in source strength (Figure 2).

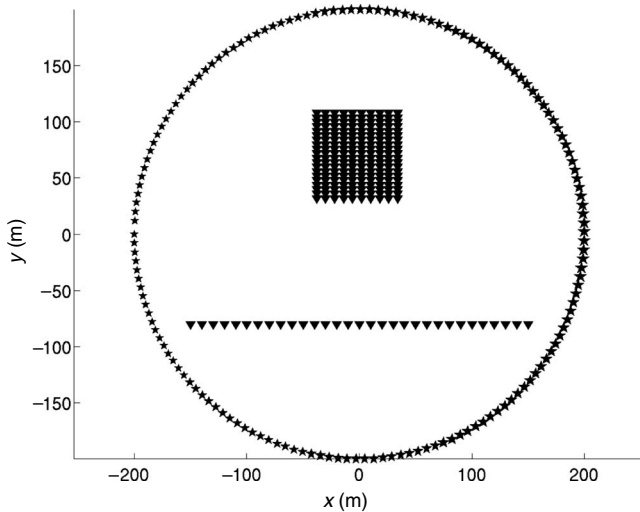


Figure 2. Source (stars) and receiver (triangles) geometry for the homogeneous example. Every second boundary source and array receiver is plotted for clarity. The size of the source symbol varies with source strength, i.e., strongest source at  $[200,0]$  m and weakest at  $[-200,0]$  m. Receiver array shown in Figure 3.

### Estimating and applying correction factors

Seismic interferometry estimates superpose a causal and an acausal Green's function. In the following examples, we consider the acausal part (the part at negative times) of the interferometric estimate. Then we time reverse it (i.e., reverse the direction of the time axis) and plot the results at positive times. We do not show both acausal and causal parts because doing so would require the derivation and application of different scaling factors.

For the first example, we use a simple homogeneous medium. We model the desired source radiation pattern  $G(\mathbf{x}_1, \mathbf{x}_r)$  using interferometric modeling (van Manen et al., 2005, 2006, 2007). This allows us to model a diffraction-limited Green's function, which (as discussed above) is what we expect in an interferometric estimate. Snapshots of this radiation pattern are shown in Figure 4a. We then determine the nonuniform radiation pattern of the interferometric Green's functions by calculating  $G'(\mathbf{x}_1, \mathbf{x}_r)$  using equation 1 and taking only negative times. Snapshots of this (biased) radiation pattern (time reversed and, hence, at positive times) are shown in Figure 4b.

To estimate the scaling factor ( $C^{\text{opt}}(\mathbf{x}_1, \mathbf{k}_r)$ ), we first taper the radiation patterns in space. We use a relatively harsh spatial taper (spatial cosine tapers are applied to 90% of the array) because it provides good results in this case. A 3D Fourier transform is applied to the tapered source-radiation patterns, i.e., we transform the data to the  $f-k_x-k_y$  domain, so  $G(\mathbf{x}_1, \mathbf{x}_r)$  and  $G'(\mathbf{x}_1, \mathbf{x}_r)$  become  $G(\mathbf{x}_1, \mathbf{k}_r)$  and  $G'(\mathbf{x}_1, \mathbf{k}_r)$ , respectively. To determine a scaling factor, we divide the absolute values of  $G(\mathbf{x}_1, \mathbf{k}_r)$  by the absolute values of  $G'(\mathbf{x}_1, \mathbf{k}_r)$ . Using the absolute values ensures that the scaling factor is real valued. However, if phase and amplitude are to be corrected in another application, then a complex-valued scaling factor can be used. A small factor may be added to the denominator to stabilize the division; we use a water-level method and set the minimum level to 5% of the maximum value of the denominator (Clayton and Wiggins, 1976).

In the following, we apply the scaling factor by tapering the biased interferometric estimates  $G'(\mathbf{k}_r, \mathbf{x}_2)$  in space (using the same taper as for the radiation patterns), transforming the biased estimates into the  $f-k_x-k_y$  domain, multiplying by the scale factor (equation 31), and applying the 3D inverse Fourier transform. This gives the corrected estimates in the  $t-x-y$  domain, where  $t$  is time and where the  $x$ - and  $y$ -axes form a standard orthogonal spatial coordinate frame. Because we have corrected Green's functions across an array but our desired virtual source location is at the center of the array, we interpolate between the four central array receivers to obtain the final, unbiased estimate of  $G(\mathbf{x}_1, \mathbf{x}_2)$ .

Figure 5a shows the set of biased interferometric Green's function estimates between the central array receiver (the virtual source position) and all receivers on the receiver line in the geometry plot in Figure 3, i.e., we determine  $G'(\mathbf{x}_1, \mathbf{x}_2)$  using equation 1. The corrected Green's functions  $G''(\mathbf{x}_1, \mathbf{x}_2)$  are shown for comparison in Figure 5b, with the desired (directly modeled, unbiased) result plotted in Figure 5c. It is difficult to see any variation between these plots. Only a small portion of the boundary around the top and bottom of the boundary source array contributes to these estimates (Snieder, 2004), so the amplitude variation in Figure 5a is not particularly large.

To highlight the differences, we normalize the entire, biased, estimated gather in Figure 5a and the exact gather in Figure 5c to a maximum of one and plot the difference between these normalized gathers (zoomed plots shown in Figure 6a). We also take the difference between the corrected gather in Figure 5b and the exact gather and plot this in Figure 6b; no scaling is applied to the latter plot because the correction factor has already accounted for the amplitude imbalance. This lack of scaling illustrates the effectiveness of our method in this configuration. Note that both plots in Figure 6 are shown at twice the scale of those in Figure 5. Clearly, the proposed algorithm corrects for most of the amplitude imbalance introduced by the non-uniform source strength.

Finally, to illustrate the fit in more detail, in Figure 7 we plot a single trace from Figure 5a along with a single trace from Figure 5b (using the trace at  $x$  equal to 50 m). In Figure 7a, we use the same gather

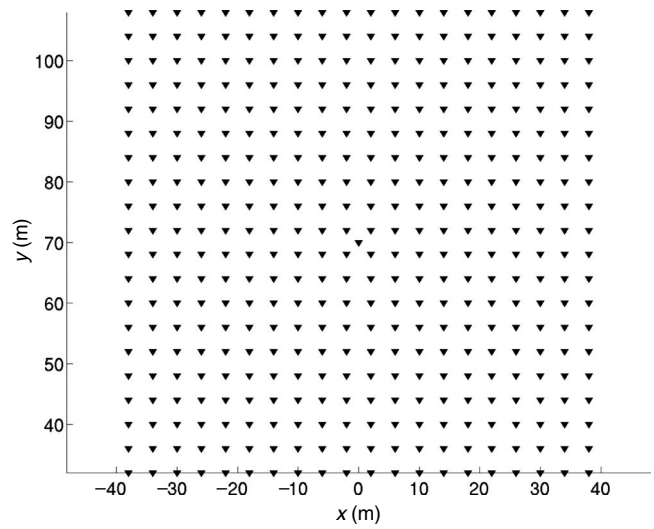


Figure 3. Details of the geometry of the receiver array.

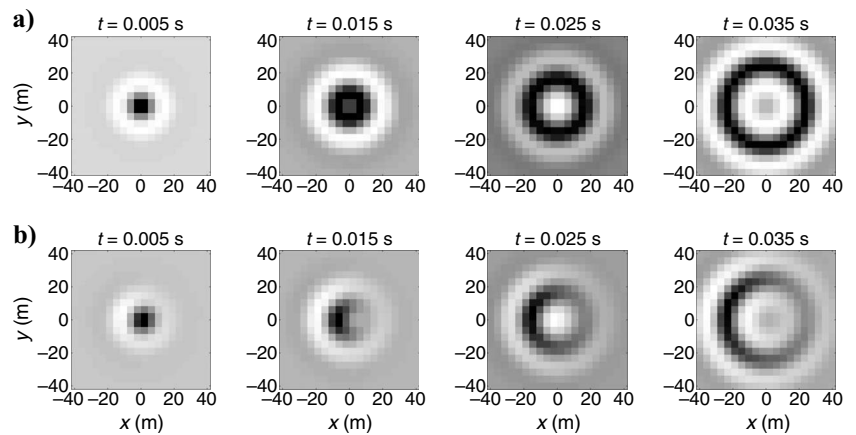


Figure 4. (a) Snapshots of the uniform radiation pattern across the virtual source array. (b) Equivalent snapshots for the nonuniform radiation pattern across the virtual source array in the homogeneous medium (see Figure 2). The center of the array is at the origin of the coordinate system.

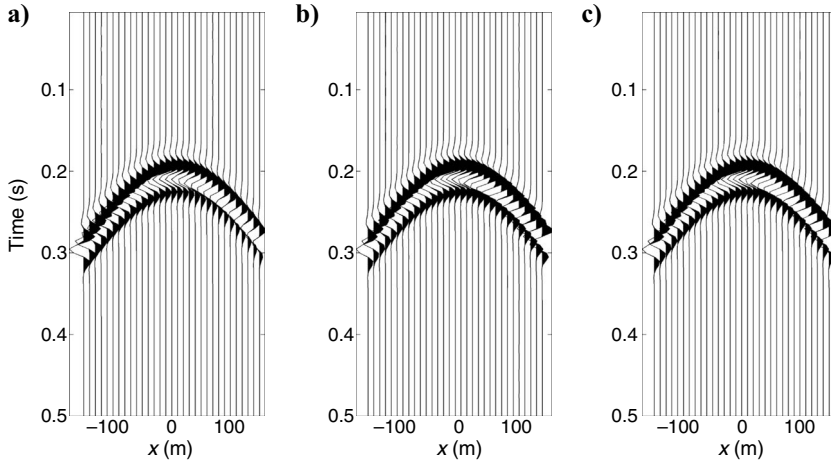


Figure 5. Results for the homogeneous medium. (a) Biased interferometric estimate, (b) corrected interferometric estimate, and (c) exact Green's functions. The virtual source is in the center of the receiver array shown in Figure 3, and the response is recorded at the line array at the bottom of Figure 3.

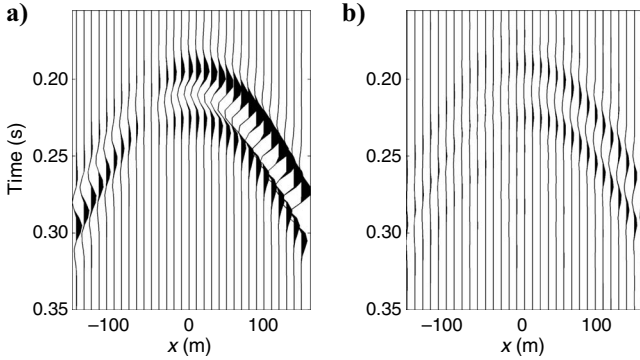


Figure 6. (a) Zoomed plot of the mismatch between gathers in Figure 5a and c after normalizing each gather to a peak amplitude of one. (b) Zoomed plot of the mismatch between gathers in Figure 5b and c (no normalization applied).

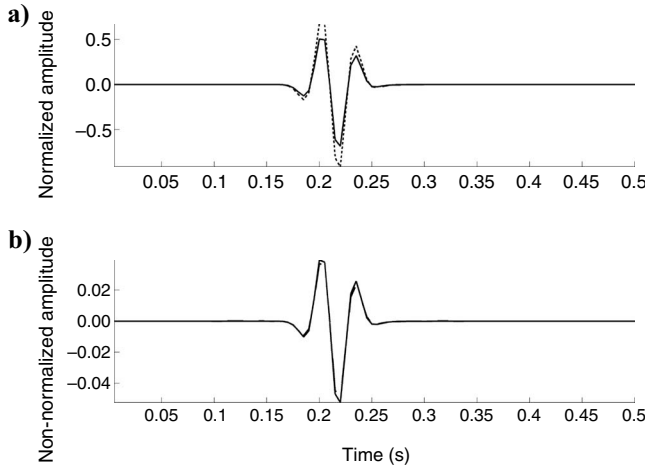


Figure 7. (a) Single trace from Figure 5a (solid line), with a single trace from Figure 5c (dashed line) for a receiver at  $x = 50$  m. Gather normalization has been applied. (b) Same as for (a) but using traces from Figure 5b and c.

normalization as in Figure 6a; the misfit can be seen clearly. No additional scaling is applied in Figure 7b, and we can note the improved fit.

In the examples we consider, if no amplitude correction is required (i.e., if the scaling function is equal to one), then tapers and stabilization factors will affect the result. In fact, correct amplitudes may be incorrectly scaled and numerical noise may be introduced by the tapers and stabilization factors. We avoid this case by ensuring that our desired radiation pattern is scaled such that it is always smaller than the biased estimates; therefore, the scale factor is never equal to one.

### Single-scatterer model

We now follow the same procedure as for the homogeneous case but use the single-scatterer model in Figure 8. To compute scattered wavefields, we use a deterministic variant of Foldy's method (Foldy, 1945; Groenenboom and Snieder, 1995; van Manen et al., 2006), where the scattering amplitude is governed by the optical theorem. We assign the imaginary part of each scatterer (there is only one in this example, but multiple scatterers are included below) an equal strength of  $-3.9$  and use the optical theorem to determine the corresponding real part of the scattering amplitude (Groenenboom and Snieder, 1995). The optical theorem ensures that both the back-scattered (reflected) and forward-scattered (transmitted) waves are modeled with the correct amplitude (which is not true in the linearized Born approximation). In Figures 9–11, we reproduce Figures 5–7 for this case. Similar to the homogeneous case, the amplitudes are well estimated by directional balancing, with only a small residual error.

We can see nonphysical arrivals prior to the first physical arrival in Figure 11a (prior to 0.1 s); these also exist in the corrected estimates in Figure 11b. The nonphysical arrivals arise from crosscorrelation of physical waves; later in this paper, we explain why these nonphysical arrivals appear in our estimates and propose two methods to identify and remove them.

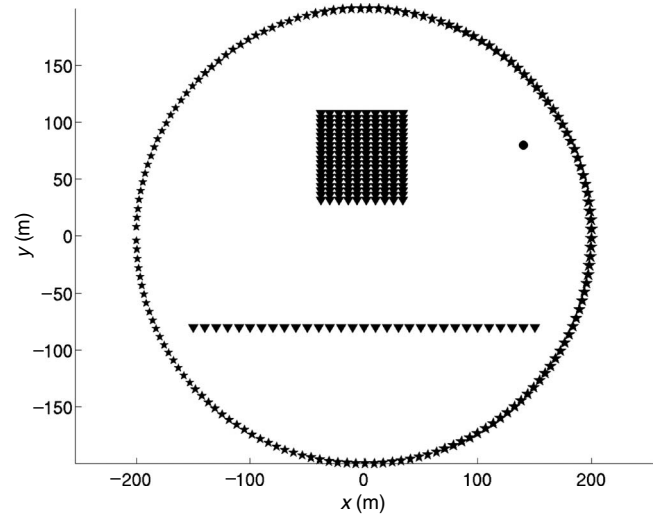


Figure 8. Single-scatterer geometry. Symbols are as for Figure 2; dot indicates the scatterer location.

### Multiple-scatterer model

We now show results of the algorithm using an example with 12 scatterers (Figure 12) in Figures 13 and 14. Here we use a slightly different receiver array, extending from  $[-120, -88]$  m to  $[120, -88]$  m with a receiver separation of 4 m. To accentuate the directional bias, the boundary source amplitude has a minimum value of one and a maximum value of four. We use a 1% water level (as opposed to the 5% discussed above) because we find that results thus improve in this case.

The same nonphysical arrivals observed in the previous section are seen here, but they are more abundant and occur at different times (prior to and after the arrival of the direct wave). These errors are also rescaled by the correction factors in the final result, so we can expect mismatches between the corrected result and the exact result. Despite this, we can see similarities between the corrected result and the exact result in Figure 13. For example, the region around 0.3–0.5 s and 0–150 m shows enhanced amplitudes with respect to the original, biased result of interferometry. These are also illustrated in the residual plot in Figure 14 (plotted at three times the scale of Figure 13), which shows that improvements have been made for the physical arrivals. In this case, however, the nonphysical arrivals are of far larger magnitude than residuals in the physical arrivals.

By comparing Figure 13c and Figure 14b, we see that some events in the residual appear to correspond to physical arrivals in the directly modeled data. Although our method assumes the latter events to be nonphysical, we observe that in more complex media it is possible that these events also contribute physical arrivals. In our examples, these arrivals are small and do not have a strong impact on the final results. However, in very complex media, these amplitudes may be larger.

Note that the nonphysical arrivals prior to the first physical arrivals are much stronger in the corrected estimate than in the biased estimate because they have been magnified by directional balancing. The balancing algorithm is designed to correct amplitudes of physically propagating waves because the correction factors are determined using only physical waves. Hence, the multiplicative correction factors are inappropriate for the nonphysical waves. We can expect that similarly magnified, nonphysical waves arrive after the first arrival but with weaker absolute amplitude (these nonphysical arrivals are related to the weaker, higher-order scattering). This explains why the residual in Figure 14b contains so much energy from the nonphysical arrivals. We now focus attention on these arrivals and show how they can be predicted and suppressed.

### NONPHYSICAL ARRIVALS

In the preceding heterogeneous examples, nonphysical arrivals are introduced in the biased interferometric estimates. We consider these nonphysical arrivals are most apparent prior to the first physical arrival, where we expect no arrivals at all (e.g., compare Figure 13a and c prior to 0.2 s). We have suggested that the residuals between the directly modeled results and the corrected results are predominantly from these nonphysical arrivals, i.e., arrivals such as

those in Figure 14b correspond to nonphysical arrivals introduced by the nonuniform amplitude distribution of the sources. We now justify this claim in more detail.

Nonphysical (sometimes called spurious) arrivals can appear in interferometric estimates when interferometry is applied in nonideal circumstances — for example, by applying interferometry using only surface sources or other spatially limited source geometries (Snieder et al., 2006; Wapenaar, 2006; Halliday and Curtis, 2008; Vasconcelos and Snieder, 2008a, 2008b) or by applying interferometry in the presence of attenuation (Wapenaar et al., 2006; Snieder, 2007; Snieder et al., 2007; Halliday and Curtis, 2009). Nonphysical arrivals introduced by nonuniform background source strengths can

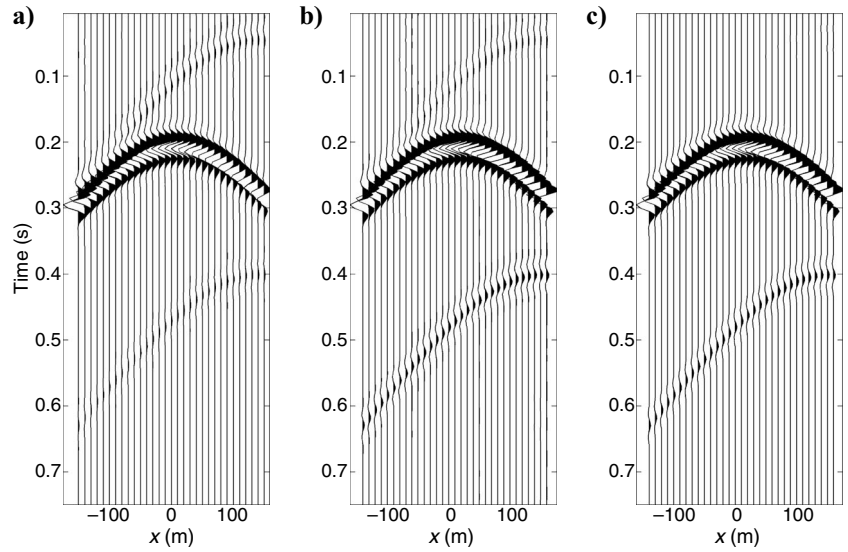


Figure 9. As for Figure 5 but for the single-scatterer example.

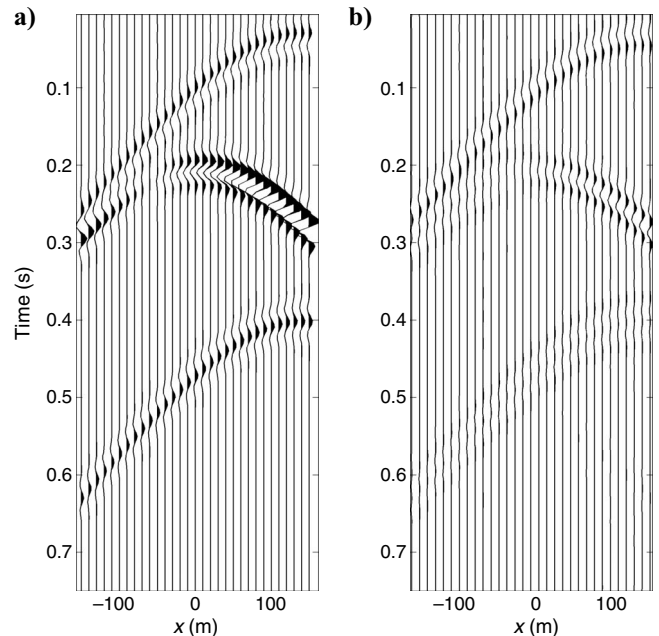


Figure 10. As for Figure 6 but for the single-scatterer example.



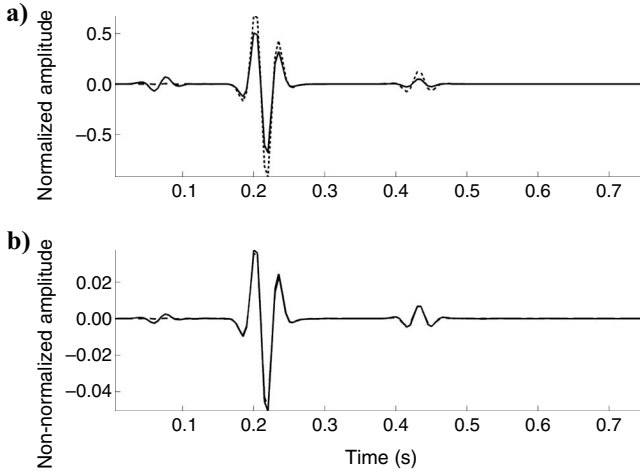


Figure 11. As for Figure 7 but for the single-scatterer example.

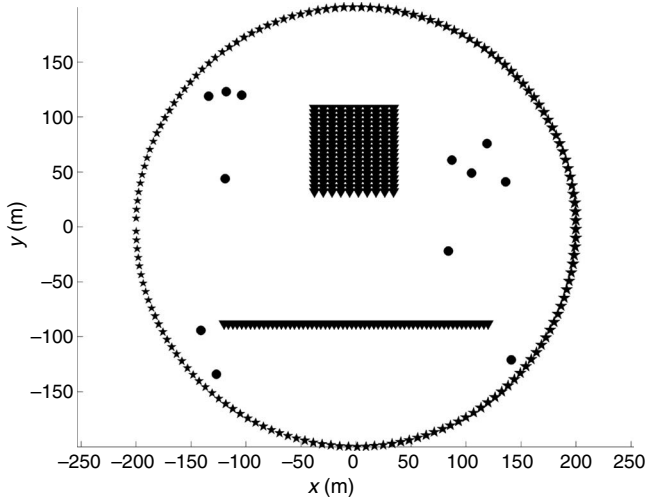


Figure 12. Geometry for the multiple-scatterer model. Symbols are as for Figure 8.

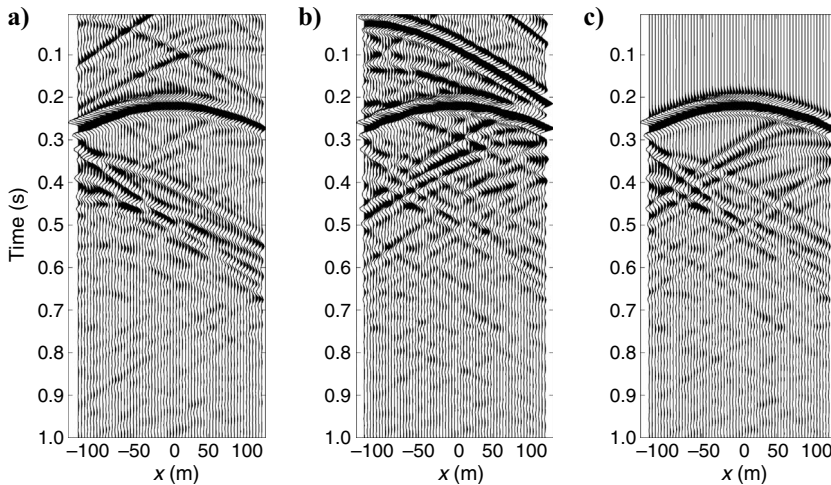


Figure 13. As for Figure 9 using the multiple-scatterer model.

be understood in a similar manner to the nonphysical arrivals introduced for surface waves by Halliday and Curtis (2009) and for acoustic waves by Snieder et al. (2008). We summarize the approach for acoustic waves here.

The wavefield at each of a pair of receivers is separated into direct waves and scattered waves before interferometry is applied, resulting in four separate contributing terms after interferometry. These are referred to as  $T1$  to  $T4$ , representing the contributions of the cross-correlation of the direct waves with the direct waves ( $T1$ ), the direct waves with the scattered waves ( $T2$ ), the scattered waves with the direct waves ( $T3$ ), and the scattered waves with the scattered waves ( $T4$ ). Similar analyses can be found using representation theorems for perturbed media (Vasconcelos et al., 2009) and for deconvolution interferometry (Vasconcelos and Snieder, 2008a, 2008b).

We first define the direct and scattered wavefields between the receiver locations  $\mathbf{x}_1$  and  $\mathbf{x}_2$  as  $G^0(\mathbf{x}_1, \mathbf{x}_2)$  and  $G^{\text{scat}}(\mathbf{x}_1, \mathbf{x}_2)$  and assume that we want to estimate these wavefields using interferometry. Terms  $T1$ – $T4$  provide the following contributions to this estimate:

$$T1 = G^{0*}(\mathbf{x}_1, \mathbf{x}_2) - G^0(\mathbf{x}_1, \mathbf{x}_2), \quad (4)$$

$$T2 = G^{\text{scat}*}(\mathbf{x}_1, \mathbf{x}_2) + G^{\text{np1}}(\mathbf{x}_1, \mathbf{x}_2), \quad (5)$$

$$T3 = -G^{\text{scat}}(\mathbf{x}_1, \mathbf{x}_2) + G^{\text{np2}}(\mathbf{x}_1, \mathbf{x}_2), \quad (6)$$

$$T4 = -G^{\text{np1}}(\mathbf{x}_1, \mathbf{x}_2) - G^{\text{np2}}(\mathbf{x}_1, \mathbf{x}_2). \quad (7)$$

The terms  $G^{\text{np1}}(\mathbf{x}_1, \mathbf{x}_2)$  and  $G^{\text{np2}}(\mathbf{x}_1, \mathbf{x}_2)$  represent the nonphysical parts of terms  $T2$  to  $T4$ . For the acoustic case, Snieder et al. (2008) show that when interferometry is applied exactly (i.e., application of equation 1 using a nonbiased closed boundary of sources), these nonphysical terms cancel when all four terms are summed, and the direct and scattered waves are recovered as desired.

However, if we consider a nonuniform source-strength distribution, then the amplitudes of the four different terms will vary and the nonphysical arrivals will not necessarily cancel, explaining why nonphysical arrivals are observed in interferometric estimates. We expect that the amplitudes of the physical parts of the estimate [i.e., the biased estimates  $G^{*0}(\mathbf{x}_1, \mathbf{x}_2)$  and  $G^{\text{scat}}(\mathbf{x}_1, \mathbf{x}_2)$ ] can be corrected using our directional-balancing algorithm (provided that the local earth model at the virtual source is correct) but that a separate, additional approach may be required to mitigate for noncancellation of these nonphysical terms.

In the remainder of this article, we present two methods with the potential to predict and isolate the nonphysical terms so they can be removed from the interferometrically constructed Green's functions.

### Wavefield-separation-based method

In a first method, we predict the nonphysical arrivals by assuming that the wavefield can be separated into two components (direct and scattered waves) and crosscorrelate only the scattered waves to find an estimate for  $T4$ . Scattered-wavefield separation methods are used by several authors to apply and analyze seismic interferometry (Snieder et al., 2008; Vasconcelos and Snieder,

2008a, 2008b; Halliday and Curtis, 2009; Vasconcelos et al., 2009). To test the potential of this method, we model the synthetic wavefield in two steps: first determining  $G^0$  and then determining  $G^{\text{scat}}$ , allowing us to calculate the four terms above explicitly. In practice, these would have to be separated in real data using time windowing,  $f$ - $k$  filtering, or some other wavefield-separation scheme. We illustrate the two different parts of the wavefield in Figure 15, where we plot the direct waves between the center point of the virtual source array and the receiver line and the corresponding scattered waves.

Separating the modeling steps allows us to calculate interferometric estimates as defined by equations 4–7, i.e., we carry out the interferometric estimation process four times, using different input wavefields at each receiver location. Each of these four estimates using the nonuniform source strength is shown in Figure 16. Figure 16a shows the result of interferometry using the direct waves recorded at the first (virtual source) and second receivers ( $T1$ ). Figure 16b shows the result of interferometry using the direct waves recorded at the first receiver and the scattered waves recorded at the second receiver ( $T2$ ). Figure 16c shows the result of interferometry using the scattered waves recorded at the first receiver and the direct waves recorded at the second receiver ( $T3$ ). And Figure 16d shows the result of interferometry using the scattered waves recorded at the first and second receivers ( $T4$ ). Summing these four gathers results exactly in Figure 13a. If the source-strength distribution were uniform, we would expect the summation of the four gathers to give the exact result (Figure 13c).

We apply the nonuniform directional balancing to each of these four results in turn using the same bespoke, or tailored, scaling factors in each case, and plot the equivalent corrected seismograms in Figure 17. In this configuration of source, receiver, and scatterer locations, the dominant contribution to the interferometric estimates comes from Figure 17a and b; Figure 17c and d predominantly contains nonphysical arrivals. Thus, by applying interferometry using separated wavefields, we create estimates of the direct waves, scattered waves, and nonphysical arrivals.

In Figure 18, we compare the residual shown in Figure 14b with the nonphysical arrival in Figure 17d. The residual is similar to the nonphysical arrivals, justifying our earlier claim that the residual is dominated by nonphysical arrivals. By estimating the nonphysical arrivals using wavefield separation, we can estimate the residual that remains in the directionally balanced interferometric estimate.

### Symmetry-based methods

An alternative approach to identify nonphysical arrivals is to use the moveout of waves across source and receiver arrays. By studying the nature of the stationary points that contribute to the nonphysical arrivals, we find that these arrivals are nonreciprocal. That is, although reversing the role of virtual source and receiver (i.e., reversing the order of crosscorrelation) in interferometry does not affect the synthesis of the physical arrivals because of source-receiver reciprocity, it does time reverse the nonphysical arrivals. (In Appendix A, we prove this using representation theorems for perturbed media [Vasconcelos et al., 2009].) Where appropriate receiver geometries exist (any geometry that allows us to observe moveout), we can use this property to construct an additional method to identify nonphysical arrivals.

We illustrate the difference in moveout between physical and nonphysical waves using a two-scatterer model. To ensure these results

are not confounded with directional effects, we use a uniform source-strength distribution around the boundary for this example. We use separated wavefields (as above) and calculate  $T2$ ,  $T3$ , and  $T4$  explicitly. In what follows, various combinations of these terms are then summed to obtain the exact (scattered) result, and to focus on nonphysical arrivals. A line of receivers with 2-m separation is used to synthesize interreceiver Green's functions (Figure 19). We begin

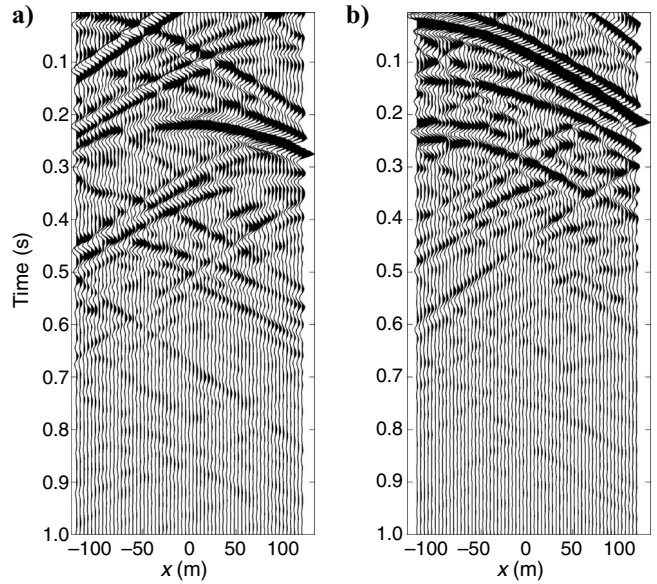


Figure 14. As for Figure 10 but using the multiple-scatterer model, and here plotted at three times the scale of Figure 13.

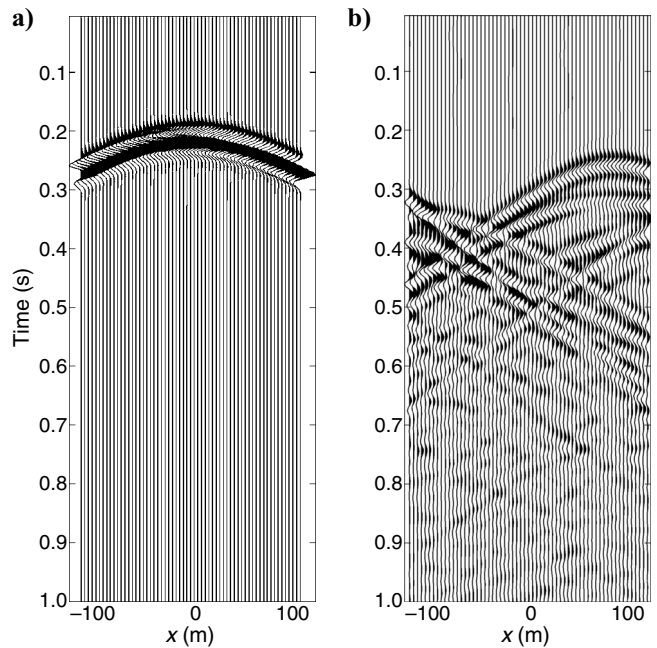


Figure 15. (a) Directly modeled direct wavefield between the central receiver of the virtual source array and the receiver line. (b) The equivalent directly modeled scattered wavefield.

by fixing the central receiver as the virtual source and calculate the Green's functions between this virtual source and all other receiver locations.

In Figure 20a, we plot the sum of terms  $T_2$ ,  $T_3$ , and  $T_4$  for a virtual source located at the center of the receiver line, with receivers at all other locations. This results in the exact virtual source-receiver scattered waves (subject to small numerical implementation errors). Note that we have used displacement rather than pressure Green's functions, so we obtain the difference between the Green's functions at positive and negative times.

This result would be the same if we had reversed the role of virtual source and receiver. In Figure 20b, we plot only the sum of terms  $T_2$  and  $T_3$ , resulting in noncancellation of the nonphysical term. We illustrate the nonreciprocal nature of the nonphysical term by switching the role of virtual source and receiver for each interferometric estimate. This result is shown in Figure 20c; although the physically scattered waves (Figure 20a) are unchanged because of reciprocity, the nonphysical arrivals have been time reversed.

To illustrate how we can further isolate these nonphysical arrivals, in Figure 21a we plot the sum of Figure 20b and c, and in Figure 21b we plot the difference between Figure 20b and c. In Figure 21a, the physical arrivals sum constructively; but in Figure 21b, the physical

arrivals cancel out, leaving the remaining nonphysical arrivals, which (apart from phase differences) match those in Figure 21a.

Hence, in addition to the wavefield-separation technique, symmetry-based methods can be used to create complementary indicators of which interreceiver arrivals are nonphysical. Presumably in real data examples, the existence of two methods will help ensure robustness of the identification process. In the rest of this article, we use the wavefield-separation method.

## REMOVING NONPHYSICAL ARRIVALS

Given methods to predict which arrivals are nonphysical, we can treat such arrivals as noise. This noise is superimposed on the real signal (the directionally balanced Green's function estimates), so the remaining problem is one of signal and noise separation. We now present results of implementing this noise removal problem.

We use a 2D  $(x, t)$  least-squares filter to match the predicted nonphysical arrival in Figure 18b to the result of the correction algorithm (Figure 13b). The direct arrival is dominant, so we remove it from the problem (i.e., we sum only Figure 17b and d; the result of the summation is shown in Figure 22a). We use 2D helical filters (Claerbout, 1998), measuring length 5 in the time direction and length 3 in the  $x$ -direction. These filters are applied in overlapping windows of 10 traces. Least-squares filtering results appear in Figure 22b. Figure 22c shows the same result, but we mute any arrivals prior to the arrival time of the direct wave because we know these arrivals cannot be physical. This allows the result to be compared to the directly modeled scattered waves shown in Figure 22d, illustrating that a large part of the nonphysical energy has been removed while the physical energy remains relatively unaffected.

Note that we have succeeded in suppressing the dominant nonphysical arrivals, which move out in the positive direction; yet the nonphysical arrivals with conflicting dips have not been suppressed. This is likely to be because these unsuppressed arrivals are weaker than the arrivals that have been suppressed, resulting in the least-squares filtering being dominated by the higher-amplitude arrivals.

It might be possible for experienced signal processors to better filter the nonphysical arrivals dipping in the positive direction and those dipping in the negative direction. The nonphysical arrival estimate could be split into positive and negative velocities, and these could be removed individually using least-squares filters — for example, using curvelet-domain filtering (Hermann et al., 2008).

Finally, we combine the different processing steps. In Figure 23, we show the original Green's function estimates using the nonuniform source strength, the result of the directional balancing algorithm, the result of the adaptive subtraction of the nonphysical arrivals, and the directly modeled result. We have subtracted the nonphysical arrival from the entire wavefield (rather than from the scattered wavefield only, as shown in Figure

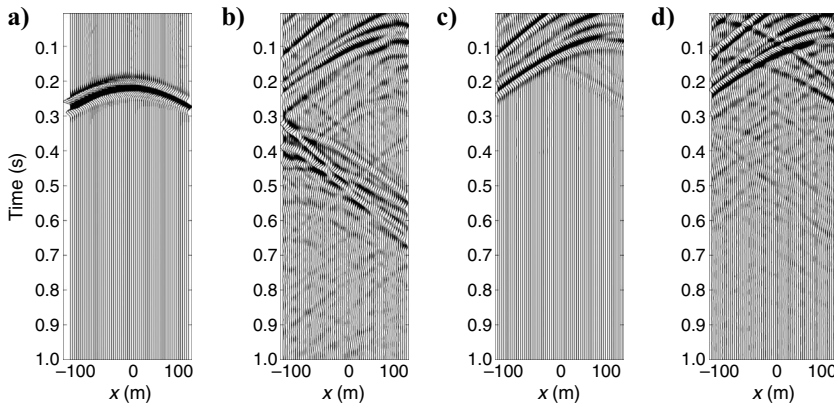


Figure 16. Interferometry applied to separated wavefields using a nonuniform source strength. (a) Direct waves crosscorrelated with direct waves, (b) direct waves crosscorrelated with scattered waves, (c) scattered waves crosscorrelated with direct waves, and (d) scattered waves crosscorrelated with scattered waves.

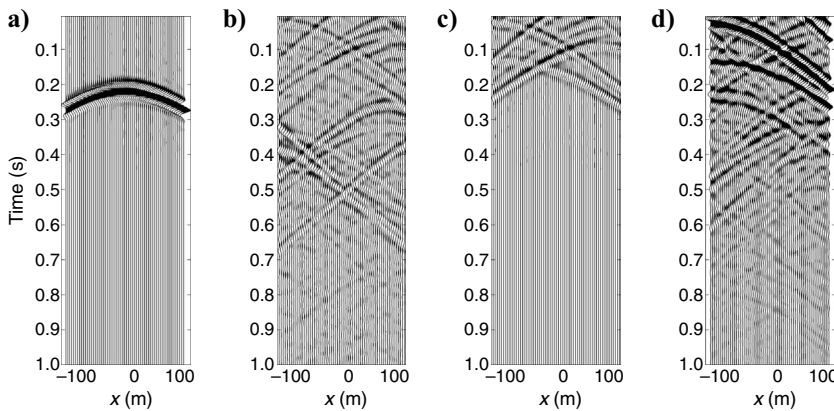


Figure 17. As for Figure 16, with directional balancing applied.



22b). As we move through the views, we see that the interferometric estimates more closely resemble the directly modeled (desired) Green's function in Figure 22d.

## DISCUSSION

Using acoustic scattering examples, we have illustrated the application of a new algorithm to correct for directional bias resulting from nonuniform source-strength distribution in seismic interferometry. Although these examples illustrate the method, challenges remain before the algorithm can be applied to correct for bias in seismic interferometry applied to real data, especially for the improved recovery of body-wave arrivals.

In our examples, the method is applied to cases where the boundary of sources is totally enclosing and well sampled. In many applications, this configuration will not exist, the source-strength distribution is not likely to be smooth, and the strength of some sources will drop to zero, resulting in gaps in the radiation pattern of the virtual source. In heterogeneous media, we would expect scattered waves to act as secondary sources to fill the gaps in the source boundary; nevertheless, it remains to be seen how stable the algorithm is in the presence of a limited source boundary. In cases where the method does remain stable when correcting for directional bias resulting from gaps in the source boundary, it may be useful when applying interferometry using passive and active sources.

We also use relatively large arrays in our examples. The array used is not optimized in any way. In practice, it may be possible to find an optimized array design that provides a sensitivity to many directional components using fewer receivers. The use of a 2D array also means that the method can only be applied exactly to waves propagating in two dimensions. For example, this configuration could be used when receivers are placed on the surface of the earth to construct interreceiver surface-wave seismograms. However, the potential of methods such as this is that they can correct for bias in reflected wavefields, allowing conventional imaging and inversion algorithms to be applied to the interferometric estimates as if they were conventional source-receiver records. It seems likely that in 3D media, 2D arrays at the surface of the earth could allow a slowness transform to distinguish waves arriving at different angles to the horizontal. Hence, correction factors can be applied to reflections as a function of 3D directions of arrival.

The modeling step used in the algorithm is very important. If the model is wrong, then the directional correction algorithm will fail. However, because the model is only required for the region of the earth immediately at the receiver array, it is far easier to constrain than larger earth models. We only model the first few time steps in the area immediately around the receiver (virtual source) array, so the modeling step is not particularly time consuming or computationally expensive.

In the steps used to remove the nonphysical arrivals from our corrected estimates, we use a method that takes advantage of separated direct and scattered wavefields. In practical applications, this requires that we separate the direct wave from the scattered (or reflected) wavefields. In the presence of dispersion and multiple scattering, this separation process may not be straightforward; however, we expect that in most cases a

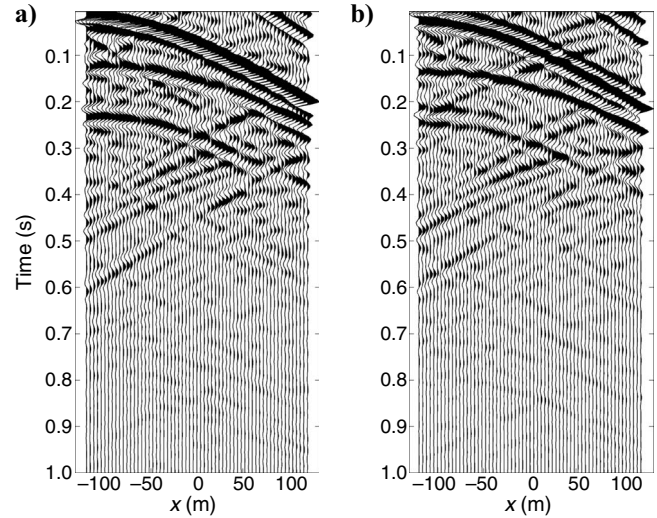


Figure 18. (a) Residual from Figure 14b (b) Nonphysical term ( $T_4$ ) from Figure 17d.

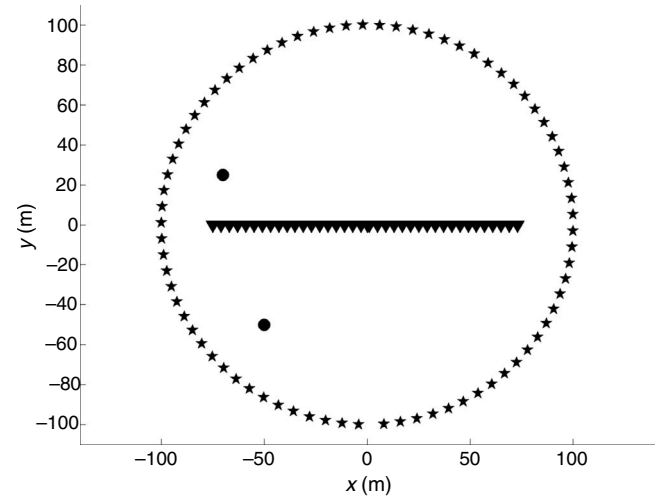


Figure 19. Geometry of the two-scatterer model. Only every second source and receiver are shown. Symbols are as for Figure 8.

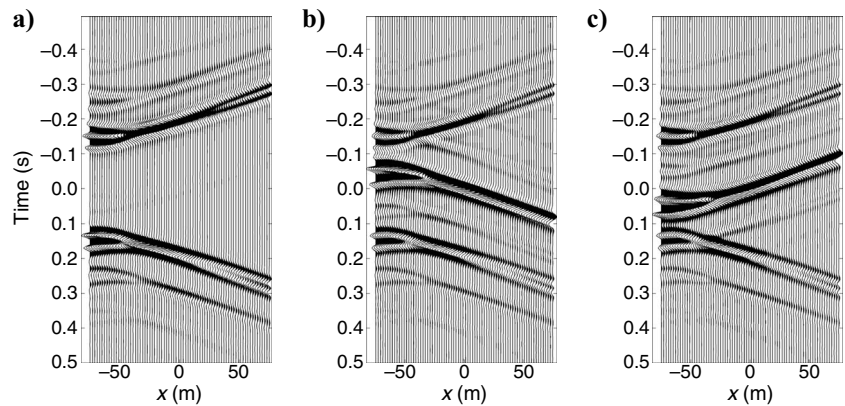


Figure 20. (a) Exact scattered surface waves determined using interferometry. Scattered surface waves, including uncanceled nonphysical terms using (b) a fixed virtual source and (c) a fixed receiver.



combination of  $f-k$  (or  $f-x$ ) filtering and time windowing would allow for an adequate estimate of the direct wave to be separated from the scattered wavefield.

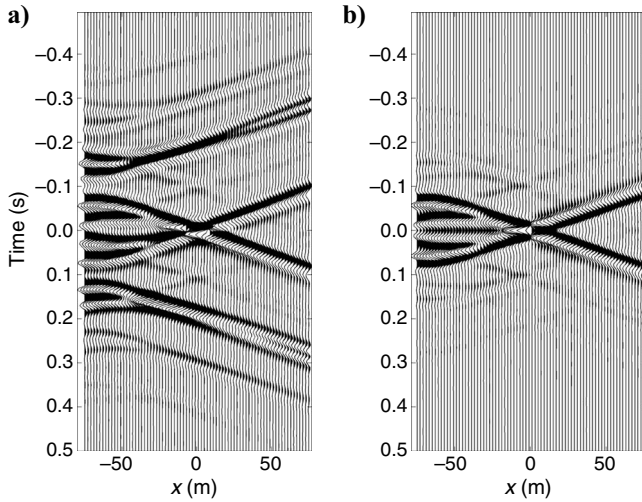


Figure 21. (a) Sum of Figure 20b and c; (b) difference of Figure 20b and c.

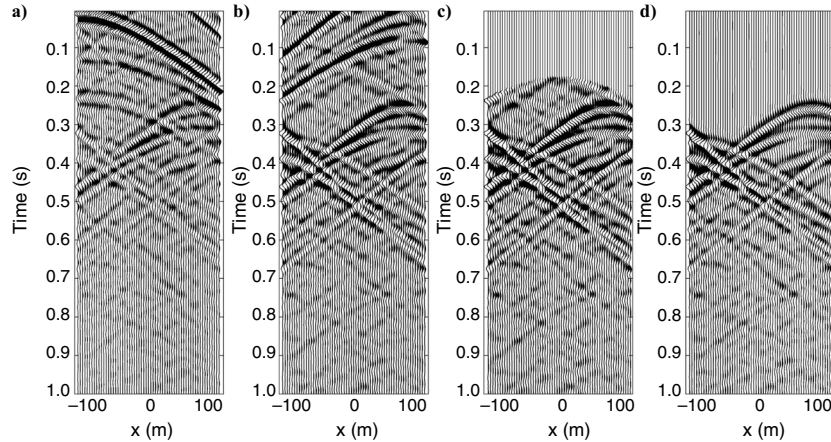


Figure 22. (a) Result of the directional balancing algorithm after removing the direct arrivals, (b) result of 2D helical least-squares filtering, (c) result in (b) but with any arrivals prior to the direct wave muted, and (d) the exact result.

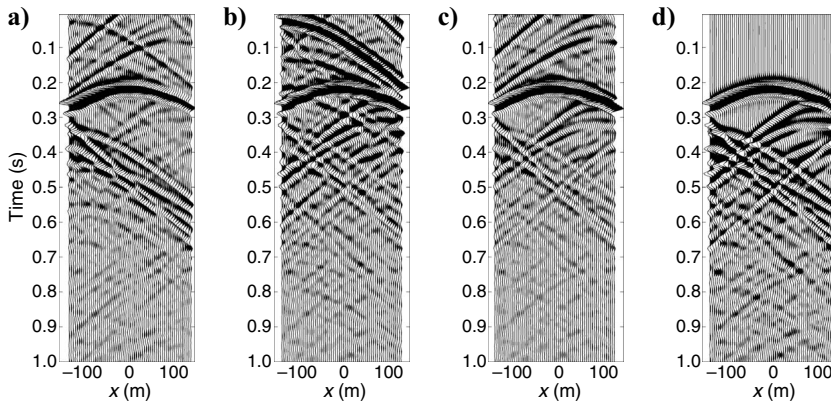


Figure 23. Complete gathers for (a) the nonuniform Green's function estimate, (b) the estimate in (a) after applying directional balancing, (c) the result of adaptive subtraction of the nonphysical arrivals, and (d) the directly modeled Green's functions.

Finally, we note that the forward-modeling steps of the directional balancing algorithm may in fact approximately account for any other errors that cause the interferometric Green's function to be inconsistent with an exact, synthetic source radiating from the virtual source point. This may, for example, correct errors incurred from approximations involved in using the monopolar version of the exact equation 1. It is also possible to use different source radiation patterns in the forward-modeling process. Thus, the directional-balancing algorithm may also allow interferometric estimates to be processed to represent cases using those different radiation patterns (for example, the balancing algorithm could steer the virtual source radiation in certain directions or give the source a particular radiation character, e.g., that of a dipole rather than monopole source).

## CONCLUSIONS

Our directional-balancing algorithm corrects interferometric estimates that are biased because of a nonuniform pattern of virtual source directionality. In our implementation, we also have used interferometry in the forward-modeling step of the directional balancing algorithm. The modeling results are thus diffraction limited and

can be compared directly to the data-derived interferometric Green's functions estimates. To illustrate the method, we have used a series of examples of varying complexity. The directional-balancing algorithm provides better interferometric estimates of the Green's functions in that they are closer to the true source-receiver data and hence more suitable for seismic data processing and inversion. Although we have considered acoustic-wave propagation, the algorithm can be applied to other wave-propagation regimes, including elastic- and electromagnetic-wave propagation. The examples shown here only consider amplitude anomalies; further work will include analyzing the algorithm's ability to correct for discrepancies in phase and amplitude.

The dominant residual after application of the algorithm consists of arrivals from nonphysical waves. We cast the remaining problem as one of signal and noise separation, where we refer to physical arrivals as signal and nonphysical arrivals as noise. We illustrated this signal and noise separation problem using a simple 2D least-squares filter. Dominant nonphysical arrivals dipping in the positive  $x$ -direction are suppressed, preserving the physical arrivals with which they interfere.

Finally, our analysis of nonphysical arrivals shows that the moveout of the physical arrivals is different to the moveout of the nonphysical arrivals — in particular, the former do not satisfy reciprocity with respect to exchange of sources and receivers. This difference in moveout is even more apparent when it is observed over two (spatial) dimensions. Hence, we expect that 3D  $(x, y, t)$  filters should provide better removal of the nonphysical arrivals.

## ACKNOWLEDGMENTS

We thank Deyan Draganov, Ivan Vasconcelos, Xander Campman, and an anonymous reviewer for valuable comments that helped to improve the manuscript. We acknowledge the support from the Scottish Funding Council for the Joint Research Institute with the Heriot-Watt University, which is part of the Edinburgh Research Partnership in Engineering and Mathematics (ERPem).

## APPENDIX A

## ON THE NONRECIPROCAL NATURE OF NONPHYSICAL ARRIVALS

In the main text, we illustrate that nonphysical arrivals relating to correlations of direct and scattered waves are nonreciprocal. When the source and receiver position are interchanged, the physical arrivals remain the same but the nonphysical arrivals are time reversed.

We can explain this observation using representation theorems for perturbed acoustic media (Vasconcelos et al., 2009). A representation theorem for lossless scattering in acoustic media can be written as

$$\begin{aligned} G_S(\mathbf{x}_1, \mathbf{x}_2) = & \oint_S \frac{1}{j\omega\rho} [G_S(\mathbf{x}_1, \mathbf{x}) \partial_i G_0^*(\mathbf{x}_2, \mathbf{x}) \\ & + \partial_i G_S(\mathbf{x}_1, \mathbf{x}) G_0^*(\mathbf{x}_2, \mathbf{x})] n_i d^2 \mathbf{x} \\ & + \oint_V \frac{1}{j\omega\rho} G(\mathbf{x}_1, \mathbf{x}) W(\mathbf{x}) G_0^*(\mathbf{x}_2, \mathbf{x}) d^3 \mathbf{x}, \end{aligned} \quad (\text{A-1})$$

where  $W(\mathbf{x})$  is the scattering potential,  $G_0(\mathbf{x}_2, \mathbf{x})$  is the wavefield in the background medium, and  $G_S(\mathbf{x}_1, \mathbf{x}_2)$  is the scattered wavefield. Rearranging, we find

$$\begin{aligned} G_S(\mathbf{x}_1, \mathbf{x}_2) - & \oint_V \frac{1}{j\omega\rho} G(\mathbf{x}_1, \mathbf{x}) W(\mathbf{x}) G_0^*(\mathbf{x}_2, \mathbf{x}) d^3 \mathbf{x} \\ = & \oint_S \frac{1}{j\omega\rho} [G_S(\mathbf{x}_1, \mathbf{x}) \partial_i G_0^*(\mathbf{x}_2, \mathbf{x}) \\ & + \partial_i G_S(\mathbf{x}_1, \mathbf{x}) G_0^*(\mathbf{x}_2, \mathbf{x})] n_i d^2 \mathbf{x}. \end{aligned} \quad (\text{A-2})$$

The right-hand side of expression A-2 is very similar to equation 1. However, here we crosscorrelate direct waves at one receiver with scattered waves at the other, i.e., this is equivalent to term T2 in the main text, where the nonphysical part is represented by the volume integral on the left side of equation A-2.

From Vasconcelos et al. (2009), we can also find a representation theorem for  $G_S^*(\mathbf{x}_1, \mathbf{x}_2)$ :

$$\begin{aligned} G_S^*(\mathbf{x}_1, \mathbf{x}_2) = & \oint_S \frac{1}{j\omega\rho} [G_S^*(\mathbf{x}_2, \mathbf{x}) \partial_i G_0(\mathbf{x}_1, \mathbf{x}) \\ & + \partial_i G_S^*(\mathbf{x}_2, \mathbf{x}) G_0(\mathbf{x}_1, \mathbf{x})] n_i d^2 \mathbf{x} \\ & + \oint_V \frac{1}{j\omega\rho} G^*(\mathbf{x}_2, \mathbf{x}) W(\mathbf{x}) G_0(\mathbf{x}_1, \mathbf{x}) d^3 \mathbf{x}, \end{aligned} \quad (\text{A-3})$$

and again we rearrange to find a representation theorem that defines term T3:

$$\begin{aligned} G_S^*(\mathbf{x}_1, \mathbf{x}_2) - & \oint_W \frac{1}{j\omega\rho} G^*(\mathbf{x}_2, \mathbf{x}) W(\mathbf{x}) G_0(\mathbf{x}_1, \mathbf{x}) d^3 \mathbf{x} \\ = & \oint_S \frac{1}{j\omega\rho} [G_S^*(\mathbf{x}_2, \mathbf{x}) \partial_i G_0(\mathbf{x}_1, \mathbf{x}) \\ & + \partial_i G_S^*(\mathbf{x}_2, \mathbf{x}) G_0(\mathbf{x}_1, \mathbf{x})] n_i d^2 \mathbf{x}. \end{aligned} \quad (\text{A-4})$$

The combination of the volume terms on the left side of equations A-2 and A-4 is then the nonphysical arrivals such as those we observe in Figures 9 and 13, i.e.,

$$\begin{aligned} G_{np1}(\mathbf{x}_1, \mathbf{x}_2) + G_{np2}(\mathbf{x}_1, \mathbf{x}_2) = & \oint_V \frac{-1}{j\omega\rho} [G(\mathbf{x}_1, \mathbf{x}) W(\mathbf{x}) G_0^*(\mathbf{x}_2, \mathbf{x}) \\ & + G^*(\mathbf{x}_2, \mathbf{x}) W(\mathbf{x}) G_0(\mathbf{x}_1, \mathbf{x})] d^3 \mathbf{x}. \end{aligned} \quad (\text{A-5})$$

When we exchange source and receiver (as we do in Figure 20), we find

$$G_{np1}(\mathbf{x}_1, \mathbf{x}_2) + G_{np2}(\mathbf{x}_1, \mathbf{x}_2) = G_{np1}^*(\mathbf{x}_2, \mathbf{x}_1) + G_{np2}^*(\mathbf{x}_2, \mathbf{x}_1). \quad (\text{A-6})$$

Hence, the nonphysical terms are nonreciprocal: the complex conjugation on the right of equation A-6 shows that interchanging the source and receiver locations changes the observed wavefield by time-reversing the nonphysical waves (leaving the physical waves unchanged by source-receiver reciprocity). By using the representation theorems for perturbed media of Vasconcelos et al. (2009), we have explained our observation in the main text that the nonphysical part of the scattered-wave estimate is nonreciprocal.

## REFERENCES

- Bakulin, A., and R. Calvert, 2004, Virtual source: New method for imaging and 4D below-complex overburden: 74th Annual International Meeting, SEG, Expanded Abstracts, 2477–2480.
- , 2006, The virtual source method: Theory and case study: Geophysics, **71**, no. 4, S1139–S1150.
- Born, M., and E. Wolf, 1999, Principles of optics: Cambridge University Press.
- Claerbout, J. F., 1968, Synthesis of a layered medium from its acoustic transmission response: Geophysics, **33**, 264–269.
- , 1998, Multidimensional recursive filters via a helix: Geophysics, **63**, 1–13.
- Clayton, R. W., and R. A. Wiggins, 1976, Source shape estimation and deconvolution of teleseismic bodywaves: Geophysical Journal of the Royal

- Astronomical Society, **47**, 151–177.
- Curtis, A., P. Gerstoft, H. Sato, R. Snieder, and K. Wapenaar, 2006, Seismic interferometry — Turning noise into signal: The Leading Edge, **25**, 1082–1092.
- de Rosny, J., and M. Fink, 2002, Overcoming the diffraction limit in wave physics using a time-reversal mirror and a novel acoustic sink: Physical Review Letters, **89**, 124301.
- Dong, S., R. He, and G. Schuster, 2006, Interferometric prediction and least squares subtraction of surface waves: 76th Annual International Meeting, SEG, Expanded Abstracts, 2783–2786.
- Douma, H., and R. Snieder, 2006, Correcting for bias due to noise in coda wave interferometry: Geophysical Journal International, **164**, 99–108.
- Draganov, D., K. Wapenaar, W. Mulder, J. Singer, and A. Verdel, 2007, Retrieval of reflections from seismic background-noise measurements: Geophysical Research Letters, **34**, L04305.
- Foldy, L. L., 1945, The multiple scattering of waves. I. General theory of isotropic scattering by randomly distributed scatterers: Physical Review, **67**, 107–119.
- Groenenboom, J., and R. Snieder, 1995, Attenuation, dispersion and anisotropy by multiple scattering of transmitted waves through distributions of scatterers: Journal of the Acoustical Society of America, **98**, 3482–3492.
- Halliday, D. F., and A. Curtis, 2008, Seismic interferometry, surface waves and source distribution: Geophysical Journal International, **175**, 1067–1087.
- , 2009, Seismic interferometry of scattered surface waves in attenuative media: Geophysical Journal International, **178**, 419–446.
- Halliday, D. F., A. Curtis, and E. Kragh, 2008, Seismic surface waves in a suburban environment — Active and passive interferometric methods: The Leading Edge, **27**, 210–218.
- Halliday, D. F., A. Curtis, D.-J. van Manen, and J. Robertsson, 2007, Interferometric surface wave isolation and removal: Geophysics, **72**, no. 5, A69–A73.
- Hermann, F. J., D. Wang, and D. J. Verschuur, 2008, Adaptive curvelet-domain primary-multiple separation: Geophysics, **73**, no. 3, A17–A21.
- Mehta, K., A. Bakulin, J. Sheiman, R. Calvert, and R. Snieder, 2007, Improving the virtual source method by wavefield separation: Geophysics, **72**, no. 4, V79–V86.
- Slob, E., D. Draganov, and K. Wapenaar, 2007, Interferometric electromagnetic Green's functions representations using propagation invariants: Geophysical Journal International, **169**, 60–80.
- Slob, E., and K. Wapenaar, 2007, Electromagnetic Green's functions retrieval by crosscorrelation and cross-convolution in media with losses: Geophysical Research Letters, **34**, L05307.
- Snieder, R., 2004, Extracting the Green's function from the correlation of coda waves: A derivation based on stationary phase: Physical Review E, **69**, 046610.
- , 2007, Extracting the Green's function of attenuating heterogeneous media from uncorrelated waves: Journal of the Acoustical Society of America, **121**, 2637–2643.
- Snieder, R., K. van Wijk, M. Haney, and R. Calvert, 2008, The cancellation of spurious arrivals in Green's function extraction and the generalized optical theorem: Physical Review E, **78**, 036606.
- Snieder, R., K. Wapenaar, and K. Larner, 2006, Spurious multiples in seismic interferometry of primaries: Geophysics, **71**, no. 4, SI111–SI124.
- Snieder, R., K. Wapenaar, and U. Wegler, 2007, Unified Green's function retrieval by crosscorrelation: Connection with energy principles: Physical Review E, **75**, 036103.
- Stehly, L., M. Campillo, and N. Shapiro, 2006, A study of the seismic noise from its long-range correlation properties: Journal of Geophysical Research, **111**, B10306.
- van der Neut, J., and A. Bakulin, 2008, Estimating and correcting the amplitude radiation pattern of a virtual source: Geophysics, **74**, no. 2, SI27–SI36.
- van Manen, D.-J., A. Curtis, and J. O. A. Robertsson, 2006, Interferometric modeling of wave propagation in inhomogeneous elastic media using time reversal and reciprocity: Geophysics, **71**, no. 4, SI47–SI60.
- van Manen, D.-J., J. O. A. Robertsson, and A. Curtis, 2005, Modeling of wave propagation in inhomogeneous media: Physical Review Letters, **94**, 164301.
- , 2007, Exact wavefield simulation for finite-volume scattering problems: Journal of the Acoustical Society of America Express Letters, **122**, EL115–EL121.
- Vasconcelos, I. R., and R. Snieder, 2008a, Interferometry by deconvolution, Part 1 — Theory for acoustic waves and numerical examples: Geophysics, **73**, no. 3, SI15–SI28.
- , 2008b, Interferometry by deconvolution, Part 2 — Theory for elastic waves and application to drill-bit seismic imaging: Geophysics, **73**, no. 3, SI29–SI41.
- Vasconcelos, I. R., R. Snieder, and H. Douma, 2009, Representation theorems and Green's function retrieval for scattering in acoustic media: Physical Review E, **80**, 036605.
- Wapenaar, K., 2003, Synthesis of an inhomogeneous medium from its acoustic transmission response: Geophysics, **68**, 1756–1759.
- , 2004, Retrieving the elastodynamic Green's function of an arbitrary inhomogeneous medium by cross correlation: Physical Review Letters, **93**, 254301.
- , 2006, Green's function retrieval by crosscorrelation in case of one-sided illumination: Geophysical Research Letters, **33**, L19304.
- Wapenaar, K., and J. Fokkema, 2006, Green's function representations for seismic interferometry: Geophysics, **71**, no. 4, SI33–SI44.
- Wapenaar, K., E. Slob, and R. Snieder, 2006, Unified Green's function retrieval by cross-correlation: Physical Review Letters, **97**, 234301.
- Wapenaar, K., J. van der Neut, and E. Ruigrok, 2008, Passive seismic interferometry by multidimensional deconvolution: Geophysics, **73**, no. 6, A51–A56.